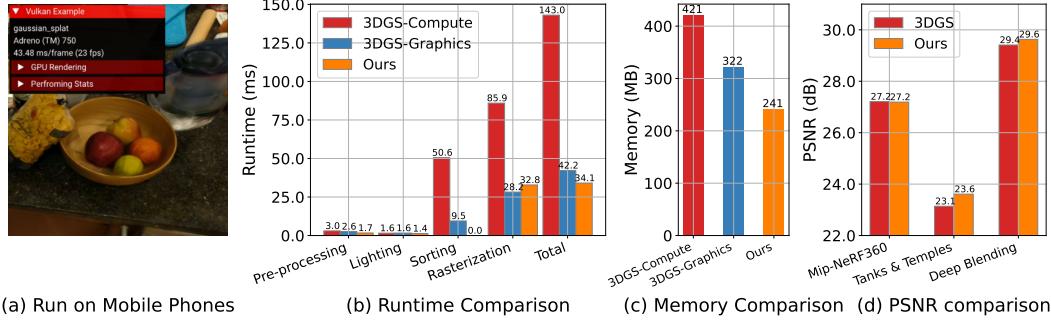# Sort-free Gaussian Splatting via Weighted Sum Rendering

Qiqi Hou[1], Randall Rauwendaal[2], Zifeng Li[2], Hoang Le[1], Farzad Farhadzadeh[1], Fatih Porikli[1],
Alexei Bourd[2], Amir Said[*1]

[1]Qualcomm AI Research[†]   [2]Graphics Research Team

[1]{qhou,rrauwend,zifeli,hoanle,ffarhadz,abourd,fporikli,asaid}@qti.qualcomm.com

| (a) Run on Mobile Phones | (b) Runtime Comparison | (c) Memory Comparison | (d) PSNR comparison |

Figure 1: This paper proposes a sort-free Gaussian Splatting method, which simplifies volumetric rendering to Weighted Sum Rendering. (a) Visual example from the "counter" scene rendered on a Snapdragon® 8 Gen 3 GPU[‡]. (b) and (c) Runtime and memory comparison between our methods and 3DGS Kerbl et al. (2023) at a resolution of 1920×1080 on the "counter" scene , respectively. We implemented two versions of 3DGS, one implementation faithfully porting 3DGS CUDA kernels to Vulkan compute shaders (3DGS-Compute), and another leveraging a global-sort following by hardware rasterization (3DGS-Graphics). (d) PSNR results on Mip-NeRF, Tank & Temples, and Deep Blending datasets.

Abstract

Recently, 3D Gaussian Splatting (3DGS) has emerged as a significant advancement in 3D scene reconstruction, attracting considerable attention due to its ability to recover high-fidelity details while maintaining low complexity. Despite the promising results achieved by 3DGS, its rendering performance is constrained by its dependence on costly non-commutative alpha-blending operations. These operations mandate complex view dependent sorting operations that introduce computational overhead, especially on the resource-constrained platforms such as mobile phones. In this paper, we propose Weighted Sum Rendering, which approximates alpha blending with weighted sums, thereby removing the need for sorting. This simplifies implementation, delivers superior performance, and eliminates the "popping" artifacts caused by sorting. Experimental results show that optimizing a generalized Gaussian splatting formulation to the new differentiable rendering yields competitive image quality. The method was implemented and tested in a mobile device GPU, achieving on average $1.23\times$ faster rendering.

1 Introduction

Photo-realistic 3D view synthesis has very wide use in graphics applications like video games, virtual reality, and 3D scene modeling techniques based on learnable appearance and transparency have achieved remarkable success thanks to their capability for consistently generating image details. Neural Radiance Fields (NeRF) by Mildenhall et al. (2021) is one seminal work using this

---

approach, where Multi-Layer Perceptron (MLP) networks and positional encoding are used to create models representing a scene's radiance field and opacity.

More recently, 3D Gaussian Splatting (3DGS) was proposed by Kerbl et al. (2023), and rapidly gained popularity (Fei et al., 2024; Chen & Wang, 2024b; Wu et al., 2024). It replaces the MLP networks used by NeRF with a sparse scattering of anisotropic 3D Gaussian "splats" that have view-dependent appearance. These splats are efficiently rendered using rasterization instead of costly volumetric ray-marching, while maintaining its rendering differentiability. Nevertheless, while 3DGS produces high quality views with significantly lower complexity compared to NeRF, it is still challenging for resource-constrained platforms like mobile phones.

An important complexity factor results from the fact that splatting volumetric elements with transparency requires sorting before α-blending, and it is difficult to combine non-commutative blending operations—which are intrinsically sequential—with the parallelization required for fast rendering. Furthermore, approximating ray integrals with sorting can create visible "popping" transitions due to temporal changes in rendering order, that can only be alleviated with more complex sorting and rendering (Radl et al., 2024).

The original 3DGS proposal achieves impressive rendering performance with a compute-based rasterizer implemented in CUDA, enabled by a tiled-based GPU radix sort that ensures front-to-back α-blending, but incurring memory overhead. Subsequent implementations have leveraged other APIs such as Vulkan or WebGL kishimisu (2024); Kwok (2024), either choosing a similar compute-based implementation, or leveraging the graphics hardware (GPU) to varying degrees. Unfortunately, there is no mechanism to feed the hardware rasterizer in a tile-wise fashion, so such implementations must either perform a costly global-sort prior to submitting work to the hardware rasterizer, or maintain a compute-based rasterizer, sacrificing the benefits of hardware execution. In the case of WebGL, implementations often rely on an asynchronous CPU-sort that runs at a lower-frequency than the frame rate, which degrades view quality and exacerbates temporal "popping" artifacts.

Although the sorting stage in Gaussian Splatting appears inevitable, it results from using approximations to physical processes. In reality, a general scheme for learning scene representations, with components and parameters optimized for the best view reproductions, is bound only by the mathematical constraints of the scene model. This observation motivates us to pursue alternative methods that reduce rendering complexity while incurring minimal degradation in view quality.

We are further encouraged by a widely adopted empirical method for rendering transparent media utilizing the traditional rendering pipeline — Order Independent Transparency (OIT) Meshkin (2007); McGuire & Bavoil (2013), representing a class of techniques in rasterization-based computer graphics for rendering transparency without sorting. By eliminating the sorting step from the rasterization pipeline, OIT maintains rendering speed and has been incorporated into commercial tools such as Blender, Vulkan, Unity, and Unreal Engine.

In this paper we exploit those approaches to develop a novel view synthesis method combining learning with commutative blending operations. It extends the definition of learned Gaussian Splatting, and integrates it with a new method for volumetric rendering, called Weighted-Sum Rendering (GS-WSR), still relying on differentiable rendering and machine learning techniques. To render an image, our approach employs the depth of each Gaussian to compute weights for each Gaussian splat using learned functions. These weighted Gaussians are then splatted onto the image plane using a straightforward summation operation, thereby obviating the necessity for sorting. As a further enhancement, we found that introducing view-dependent opacity greatly improved image quality for sort-free Gaussian Splatting.

This paper contributes to Gaussian Splatting as follows. First, we present the first sort-free Gaussian Splatting technique which is compatible with the graphics pipeline, and allows us the benefit of hardware rasterization. Second, we introduce Weighted Sum Rendering as well as view-dependent opacity that can effectively learn the model parameters and produce high-quality rendered images. Third, our experiments show that our method accelerates Gaussian Splatting with comparable visual performance on mobile phones.

2 RELATED WORK

Neural Scene Representations. Recent advancements in neural scene representations for novel view synthesis have led to significant progress, with techniques assigning neural features to structures like volumes Lombardi et al. (2019); Sitzmann et al. (2019), textures Chen et al. (2020); Thies et al. (2019), or point clouds Aliev et al. (2020). The pioneering NeRF (Neural Radiance Fields) approach Mildenhall et al. (2021), revolutionized the field by using Multi-Layer Perceptrons (MLPs) to encode 3D density and radiance without proxy geometry, achieving photorealistic renderings from sparse 2D images. Subsequent research has aimed to enhance NeRF's quality and efficiency through optimized sampling strategies Neff et al. (2021), light field-based formulations Li et al. (2022), compact representations Müller et al. (2022), tensor decomposition Chen et al. (2022), or leveraging the polygon rasterization pipeline for efficient rendering on mobile devices such as MobileNeRF Chen et al. (2023). However, the high computational and memory requirement still puts a challenge on mapping these methods on resource constrained platforms.

Order Dependent Transparency 3DGS The novel 3D Gaussian Splatting (3DGS) and its numerous follow-up works primarily utilize anisotropic 3D Gaussians for scene representation and an efficient differentiable rasterizer to project these Gaussians onto the image plane, either in pixel or feature representation Hamdi et al. (2024); Lin et al. (2024); Yu et al. (2024); Liang et al. (2024); Yan et al. (2024); Lu et al. (2024); Bulò et al. (2024); Fan et al. (2024); Fu et al. (2024); Zhang et al. (2024); Zou et al. (2024); Jiang et al. (2023); Qin et al. (2024); Li et al. (2024). These methods enable fast, high-resolution rendering while maintaining excellent quality. For a comprehensive overview, please refer to recent survey papers such as Chen & Wang (2024a). A crucial requirement in these methods for proper blending and rendering is the order of the Gaussians, which are typically sorted by their depth using a tile-based sorting algorithm. However, this sorting requirement introduces several challenges in practical implementation and visual quality, such as sudden changes in the appearance of object parts or "popping" artifacts, as recently addressed in Radl et al. (2024). While their results show a limited increase in computational complexity, the necessary sorting modifications are significantly more involved.

Order Independent Transparency. Modeling partial coverage has a long history in computer graphics. It's an essential problem as we need to render fine non-opaque structure or elements such as flames, smoke, clouds, hair, etc. In Porter and Duff's seminal work Porter & Duff (1984), they formulate transparency as the **OVER** operator as

$$\mathbf{C} = \alpha_0 \mathbf{c}_0 + (1 - \alpha_0)\mathbf{c}_1, \tag{1}$$

where α, $\mathbf{c}$ indicate alpha and color, respectively. As the **OVER** operator is not commutative, it requires back-to-front order for composition. Traditional accelerated either by successively "peeling" depth layers Everitt (2001) or accumulating list for sorting like A-buffers Carpenter (1984). These methods introduce time and memory overhead.

To avoid sorting, there are many methods that have been proposed to approximate compositing, namely Order-Independent Transparency (OIT). For instance, k-buffer methods work like depth peeling methods, but only storing and accumulating first k-layers in a single pass Bavoil et al. (2007). Alternatively, stochastic transparency methods in Monte Carlo rendering samples the fragments according to the opacity and depth, which can generate promising results for a large sampling rate Enderton et al. (2010). A survey on these methods can be found in Wyman (2016).

The weighted blended OIT proposed by McGuire & Bavoil (2013) is the most relevant to our method. There are several OIT variants listed in McGuire & Bavoil (2013), the most general of which is to replace the **OVER** operator with the following commutative blending operator

$$\mathbf{C} = \prod_{i=1}^{\mathcal{N}} (1 - \alpha_i)\, \mathbf{c}_0 + \left(1 - \prod_{i=1}^{\mathcal{N}} (1 - \alpha_i)\right) \frac{\sum_{i=1}^{\mathcal{N}} \mathbf{c}_i \alpha_i w\,(d_i, \alpha_i)}{\sum_{i=1}^{\mathcal{N}} \alpha_i w\,(d_i, \alpha_i)} \tag{2}$$

where d_i is the distance to camera, $\mathbf{c}_0$ is the background color, $w\,(\cdot)$ is a function that decreases with distance, so that objects nearer to the camera are assigned larger weights. In the OIT rendering Eq. 2 there are two sums defining pixel values, and since addition is commutative, they can be computed in any order. The final pixel value can only be computed after the two sums are known, which can be implemented as a single pass post-process over the image.
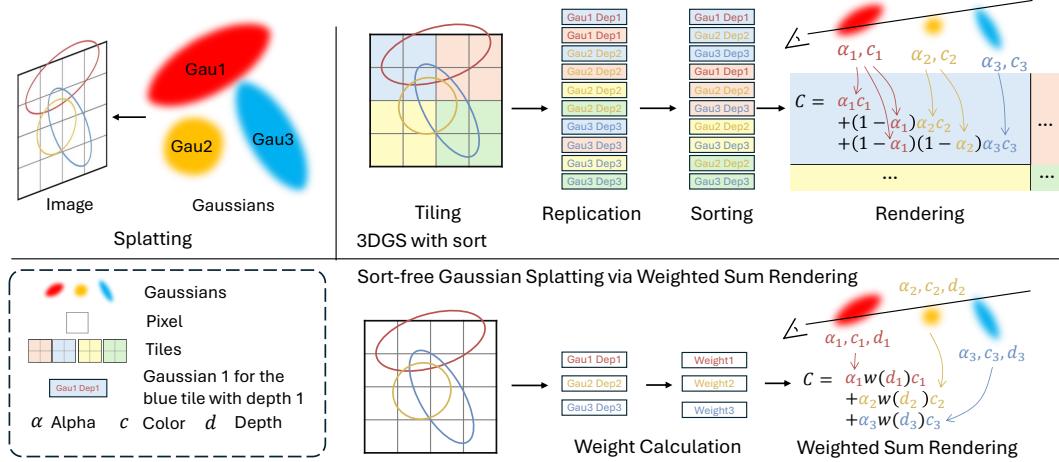
Figure 2: The architecture of sort-free Gaussian Splatting via Weighted Sum Rendering. 3DGS needs to tiling, replication, sorting, and rendering. Our method only needs to calculate the weight for each Gaussian, and independently sum their contributions per-pixel.

3 PRELIMINARIES: GAUSSIAN SPLATTING

The 3DGS scene model $\mathcal{G} = \{(\mathbf{p}_i, t_i, \mathbf{q}_i, \mathbf{s}_i, \mathbf{H}_i)\}_{i=1}^{\mathcal{N}}$ represents a scene of $\mathcal{N}$ Gaussians with center locations $\mathbf{p} \in \mathbb{R}^3$, maximum opacity $t_i \in [0, 1]$, orientation $\mathbf{q} \in \mathbb{R}^4$, scale $\mathbf{s} \in \mathbb{R}^3$, and spherical harmonics coefficients $\mathbf{H}$ following an equation similar to Gaussian probability distributions. The opacity of each element at a position $\mathbf{x}$ in 3D space is defined according to

$$\alpha_i(\mathbf{x}) = t_i \exp\left(-\frac{(\mathbf{x} - \mathbf{p}_i)^t \left[\mathbf{\Sigma}(\mathbf{q}_i, \mathbf{s}_i)\right]^{-1} (\mathbf{x} - \mathbf{p}_i)}{2}\right), \quad i = 1, 2, \cdots, \mathcal{N} \tag{3}$$

and considering a camera with focal point at position $\mathbf{f}$, the view-dependent color is defined by

$$\mathbf{c}_i = Y\left(\|\mathbf{f} - \mathbf{p}_i\|, \mathbf{H}_i\right), \quad i = 1, 2, \cdots, \mathcal{N}, \tag{4}$$

where $Y(\cdot)$ indicates the spherical harmonic function and $\|\cdot\|$ indicates the vector norm.

To render an image, each 3D Gaussian is mapped to 2D as approximated by a 2D Gaussian with the following 2×2 covariance matrix

$$\mathbf{\Sigma}_{2D} = \mathbf{J}\mathbf{W}\mathbf{\Sigma}_{3D}\mathbf{W}^t\mathbf{J}^t \tag{5}$$

where $\mathbf{W}$ is a matrix defined by the camera's image-generation transformation, and $\mathbf{J}$ is the Jacobian matrix defined by an affine approximation of the projective camera transformation.

Critically, due to it's non-commutative blending operations requiring a strict depth ordering, it is necessary to sort Gaussians according to their distance to the camera position $\mathbf{f}$. Formally, it is necessary to determine a sorting sequence $s[k]$ of indexes according to increasing depth such that

$$k \geq l \Rightarrow d_{s[k]} \geq d_{s[l]}, k, l = 1, 2, \cdots, \mathcal{N} \tag{6}$$

After sorting Gaussians in depth order, the final pixel color obtained by Gaussian splatting can be computed according to

$$\mathbf{C} = \sum_{i=1}^{\mathcal{N}} \mathbf{c}_i \alpha_i \prod_{j=1}^{i-1} (1 - \alpha_j), \tag{7}$$

which corresponds to the well-known computer graphics technique of alpha-blending (Marschner & Shirley, 2015).

4 SORT-FREE GAUSSIAN SPLATTING VIA WEIGHTED SUM RENDERING

4.1 SORT-FREE GAUSSIAN SPLATTING

As discussed in Sec. 3, 3DGS relies on non-commutative alpha blending, which requires a depth order sorting operation before rendering. To recover high-fidelity of the rendered images, 3DGS

models typically include a substantial number of Gaussians, which can escalate to millions in complex scenes. The overhead associated with these sorting operations poses a challenge in splatting Gaussians onto an image without effective optimization.

To accelerate rendering, 3DGS incorporates several optimizations designed to leverage parallel computation capabilities in CUDA. As shown in Figure 2, 3DGS splits the rendered image into multiple non-overlapping tiles, with Gaussians that span across multiple tiles being duplicated accordingly. Each Gaussian is assigned a tile ID and sorted by depth on a per-tile basis. Once sorted, all tiles are rendered in parallel, significantly improving computational efficiency. Additionally, 3DGS employs early termination to further optimize performance: if the alpha value of the frontmost Gaussians is sufficiently high, the rendering process will skip subsequent Gaussians, reducing unnecessary computations and memory usage.

While 3DGS achieved promising results, its CUDA based implementation restricts its portability, and its sorting requirement limits its performance. Their usage of an efficient tile-based radix sort forces them maintain a fully compute-based render pipeline, including compute-based rasterization. On the other hand, current APIs fail to expose efficient mechanisms to submit geometry to the hardware rasterizer in a tiled fashion, thereby requiring that implementations leveraging the hardware rasterizer execute a more costly global sort over all visible Gaussians. 3DGS chose to pursue the fully compute-based approach with its CUDA implementation, which denies them some of the benefits of the GPU's fixed function hardware. Their tile-based sort incurs some overhead in its duplication of Gaussians at tile boundaries, which is exacerbated in instances where there are a large number of Gaussians, and finally, as noted by prior work Radl et al. (2024), sorting Gaussians by their centers can introduce "popping" artifacts during view transformation, further affecting visual quality.

These limitations motivate the elimination of the sorting phase in Gaussian Splatting, which not only significantly simplifies the implementation but also enhances compatibility with hardware graphics pipelines. Inspired by Order Independent Transparency (OIT), we propose a novel approach that modifies the volumetric rendering process in 3DGS to a more efficient representation termed Weighted Sum Rendering (WSR).

4.2 Weighted Sum Rendering

Figure 2 compares the architectures of the original sort-based 3DGS model, with our proposed sort-free Gaussian Splatting framework. Unlike the volumetric rendering approach employed by 3DGS, our method estimates the transparency of each Gaussian solely based on its depth and learnable parameters, thereby eliminating the need for depth ordering. The final image can be rendered using

$$\mathbf{C} = \frac{\mathbf{c}_B w_B + \sum_{i=1}^{\mathcal{N}} \mathbf{c}_i \alpha_i w(d_i)}{w_B + \sum_{i=1}^{\mathcal{N}} \alpha_i w(d_i)}, \qquad (8)$$

where $\mathbf{c}_B$ and w_B indicate the color and learnable weight of the background, respectively. d indicates the depth. $w(\cdot)$ indicates the learnable weight function. Our network learns the Gaussian's parameters during training. Rendering with Eq. 8 in WSR cor-

Figure 3: Three variants of Weighted Sum Rendering with different weight calculations, namely Direct Weighted Sum Rendering (DIR-WSR), Exponential Weighted Sum Rendering (EXP-WSR), and Linear Correction Weighted Sum Rendering (LC-WSR).

responds to computing weighted sums. As the addition is commutative, these sums can be computed in any order, overcoming the constraints of depth sorting. Unlike traditional OIT methods Meshkin (2007); McGuire & Bavoil (2013), which rely on predefined parameters, our method optimizes the parameters of this new representation during training.

3DGS produces novel views based on a physics-based blend model, whereas GS-WSR demonstrates the benefits of departing from a phsyically-based model, and using machine learning to train the parameters for a non-physically based model. In volumetric rendering Eq. 7, it is necessary to have $\alpha_i \in [0, 1]$ to guarantee that all terms are positive. However, these constraints are not necessary in WSR Eq. 8 as α_i serves as a learnable parameter in a radiance field model. Removing such
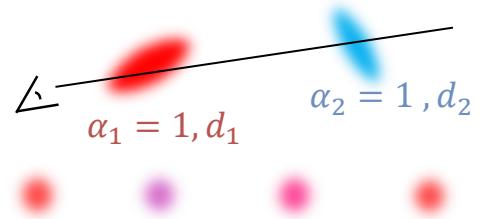
constraints can potentially result in better approximations. Similarly, our view-dependent opacity may not correspond to optical laws, but it is in practice useful for minimizing the limitations of the WSR Eq. 8 compared to volume rendering Eq. 7.

Direct Weighted Sum Rendering (DIR-WSR). A straightforward method of rendering is to sum all contributions directly, allowing the network to learn specific opacities. In DIR-WSR, the weight is defined as a constant as follows

$$w(d_i) = 1, \quad i = 1, 2, \cdots, \mathcal{N}. \tag{9}$$

However, DIR-WSR does not work well for the complex scenes, and often introduces blurring artifacts in areas where Gaussians overlap. We attribute the poor visual performance due to the lack of depth information, which prevents accurate estimation of transparency. A visual example is provided in Figure 3, illustrating two non-transparent Gaussians with $\alpha = 1$ with different color[1]. Since DIR-WSR uses a constant weight of 1, it is unable to correctly handle this situation, leading to an incorrect estimation of the resulting color as purple.

Exponential Weighted Sum Rendering (EXP-WSR). To better capture the effects of occlusion, we introduce EXP-WSR to assign larger weights to Gaussians closer to the camera. The weight is defined as

$$w(d_i) = \exp\left(-\sigma d_i^\beta\right), \quad i = 1, 2, \cdots, \mathcal{N}, \tag{10}$$

where σ, β are learnable parameters. In this manner, the Gaussians closer to the viewer would have a higher weight, thus contributing more to the final rendered image. Although EXP-WSR can effectively reduce artifacts and generate better results compared to DIR-WSR, it is not entirely free from visual distortions, as distant Gaussians still contribute to the rendered image to some extent. As shown in Figure 3, the red Gaussian, being closer to the viewer, has a larger weight than the blue Gaussian, yielding results that are closer to the ground truth. However, some artifacts remain visible in the final output.

Linear Correction Weighted Sum Rendering (LC-WSR). Inspired by the deformable convolution Dai et al. (2017) and KPConv Thomas et al. (2019), we use linear correction to estimate the weight from depth by

$$w(d_i) = \max\left(0, 1 - \frac{d_i}{\sigma}\right) v_i, \quad i = 1, 2, \cdots, \mathcal{N}, \tag{11}$$

where σ, v_i are learnable parameters. This formulation will assign a relatively larger weight for the Gaussians closer to the camera. For distant Gaussians, the weight may be reduced to 0, depending on σ or v_i. As shown in Figure 3, the rendered result is closest to the ground truth, since this model can set weights to zero it can more accurately model occlusions. Additionally, compared to EXP-WSR, LC-WSR is cheaper to compute.

4.3 VIEW-DEPENDENT OPACITY

In Sec 4.2, we proposed WSR to assign different weights to Gaussians according to their depth. Moreover, the order of Gaussians would also change depending on the viewer's direction in the original 3DGS. Figure 4 illustrates this phenomenon: two viewers observe two Gaussians from different directions. The left viewer assigns a larger weight to the red Gaussian, while the right viewer assigns a smaller weight to the same Gaussian. This observation motivates our approach to assigning view-dependent opacities.

Figure 4: View dependent opacity. In 3DGS, the accumulated $\hat{\alpha}$ changes depending on the viewer's direction, which motivates us to assign view-dependent opacities in sort-free Gaussian Splatting.

We substitute our opacity values for an additional set of spherical harmonic coefficients for view-dependency. It's another mechanism by which we mitigate the contribution of occluded Gaussians.
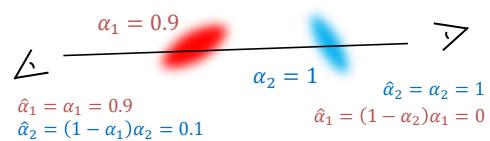
---

[1]Please note that in WSR, α can be larger than 1. We assume $\alpha = 1$ as non-transparency for illustrative purposes.

We modify Eq 3, which defines the sort-free Gaussian's opacity, replacing the 3DGS element's maximum opacity $t_i \in [0, 1]$ with an unconstrained value u_i as

$$u_i = Y\left(\|\mathbf{f} - \mathbf{p}_i\|, \mathbf{H}_i\right), \quad i = 1, 2, \cdots, \mathcal{N}, \tag{12}$$

where $Y(\cdot)$ indicates the spherical harmonic function and $\|\cdot\|$ indicates the vector norm. $\mathbf{H}_i$ indicates the learnable spherical harmonics coefficients for opacity. Thus, the maximum opacity u_i depends on view direction $\|\mathbf{f} - \mathbf{p}_i\|$ according to learned spherical harmonics parameter vector $\mathbf{H}_i$. There is a slight difference to the SH evaluation for the RGB channels and the opacity in our implementation. The maximum opacity u_i is not clamped. Please note that the view-dependent opacity may not correspond to optical laws, but it is in practice useful for minimizing the limitations of OIT rendering Eq. 8 compared to volume rendering Eq. 7.

4.4 IMPLEMENTATION DETAILS

Loss function. We optimize our sort-free Gaussian Splatting using the same rendering loss from 3DGS Kerbl et al. (2023), which contains the ℓ_1 loss and D-SSIM loss with a factor of 0.2.

Training and Evaluation. We trained our sort-free Gaussian Splatting method using PyTorch. We implemented the custom CUDA kernels for the PyTorch version. For EXP-WSR, we initialize the $\sigma = 0.1$ and $\beta = 0.8$. For LC-WSR, we initialize $\sigma = 10$ and $v_i = 0.1$. For convenience, we also evaluate the quality of our method with a PyTorch inference simulation.

Testing on mobile devices. To measure model efficiency on mobile devices, we implemented our method and the competitive 3DGS method in Vulkan [2], which is a cross-platform graphics and compute API created and maintained by the Khronos Group [3].

3DGS's rendering on mobile device contains four steps: pre-processing, lighting, sorting, and rasterization. The pre-processing step projects the 3D Gaussian into 2D based on the camera view. The lighting stage calculates per-Gaussian color based on the camera view and the spherical harmonics (SHs). The sorting step sorts the Gaussians front to back, and the rasterization step rasterizes all Gaussians within each tile to output the final image.

To make a fair comparison, we implemented two versions of 3DGS, namely 3DGS-Compute and 3DGS-Graphics. 3DGS-Compute attempts to faithfully replicate the approach from 3DGS Kerbl et al. (2023) in Vulkan compute shaders. It follows a similar scheme of replicating Gaussians per-overlapped tile, followed by compute-based rasterization. The most notable difference is that the optimized radix-sort from the NVIDIA CUB libraries NVIDIA (2024) had to be replaced with a Vulkan equivalent. By contrast, the 3DGS-Graphics approach allows for more mobile friendly execution. It's implementation globally sorts the Gaussians, eliminating per-tile replication, and allowing it to easily submit a global list of Gaussian to the hardware graphics pipeline. Gaussian color and opacity are evaluated in a fragment shader. These modifications allow Gaussians to be efficiently rendered by the fixed-function rasterizer, while their contributions are accumulated by hardware blending operations.

For both our method and the 3DGS methods, the pre-processing and lighting steps remain the same as the original 3DGS implementation, except that our method's opacity is now calculated in the lighting stage based on the camera view and SHs. Our method removes the entire sorting step, and rasterizes Gaussians in a fragment shader. Besides, our method contains an extra subpss to perform the final normalization step. With our method, all Gaussians are rendered using a single instanced draw call instead of the per-tile fashion used by 3DGS. We verified the consistency between our on mobile implementation versus the Pytorch reference implementation. Please refer to our supplementary for more details about our on mobile implementation.

5 EXPERIMENTAL RESULTS

Datasets. To ensure a fair comparison, we followed the evaluation setting of 3DGS Kerbl et al. (2023) and conducted our experiments on 13 real-world scenes. Specifically, they include the complete set of scenes from the Mip-Nerf360 dataset Barron et al. (2022), two scenes from the Tanks &

---

[2]https://www.vulkan.org
[3]https://www.khronos.org

Figure 5: Visual comparison on the Mip-NeRF 360 dataset. Our OIT method achieves similar visual performance compared to 3DGS. Please note that our method doesn't require the order of Gaussians.

Table 1: PSNR scores of our method on the Mip-NeRF360 dataset, the Tanks & Temples dataset, and the Deep Blending dataset. Our method achieved comparable results with 3DGS.

Method	Mip-NeRF 360			Tanks & Temples			Deep Blending		
	PSNR↑	SSIM↑	LPIPS↓	PSNR↑	SSIM↑	LPIPS↓	PSNR↑	SSIM↑	LPIPS↓
Plenoxels	23.08	0.626	0.463	21.08	0.719	0.379	23.06	0.795	0.510
INGP-Base	25.30	0.671	0.371	21.72	0.723	0.330	23.62	0.797	0.423
INGP-Big	25.59	0.699	0.331	21.92	0.745	0.305	24.96	0.817	0.390
M-NeRF360	**27.69**	0.792	0.237	22.22	0.759	0.257	29.40	0.901	0.245
3DGS	27.21	**0.815**	0.214	23.14	0.841	0.183	29.41	**0.903**	0.243
LC-WSR	27.19	0.804	**0.211**	**23.61**	**0.842**	**0.177**	**29.63**	0.902	**0.229**

Temples dataset Knapitsch et al. (2017), and two scenes from the Deep Blending dataset Hedman et al. (2018). These scenes encompass various challenging scenarios, including both indoor and outdoor environments.

Evaluation metrics. We evaluate reconstruction fidelity using Peak Signal-to-Noise Ratio (PSNR), Structural Similarity (SSIM), and Learned Perceptual Image Patch Similarity (LPIPS) metrics. For model efficiency, we report run times on a Qualcomm® Adreno™ GPU from Snapdragon 8 gen 3 chipset. To enable comparison, we also re-implemented our method and the official 3DGS (Kerbl et al., 2023) in Vulkan for this setting.

5.1 COMPARISON WITH STATE-OF-THE-ART METHODS

We compare our method with state-of-the-art techniques, including Plenoxels Fridovich-Keil et al. (2022), INGP Müller et al. (2022), M-NeRF360 Barron et al. (2022), and 3DGS Kerbl et al. (2023). The results in Table 1 demonstrate that our method, while avoiding any sorting, achieves comparable results to the baseline 3DGS. In terms of PSNR, our method outperforms 3DGS by 0.47dB and 0.22dB on the Tanks & Temples and Deep Blending datasets, respectively, while averaging only 0.02dB less on the Mip-NeRF360 dataset. For visual comparison, Figure 5 shows that our LC-WSR

Table 2: Runtime (ms) comparion using a Snapdragon 8 Gen 3 GPU on the Mip-NeRF360, Tanks & Temples and Deep Blending datasets. The images are rendered at a resolution of 1920×1080. When the mobile resources are exhausted, it would significantly slow down the rasterization (labeled with "*").

Method	Task	Mip-NeRF360									Tanks&Temples		Deep Blending	
		bicycle	flowers	garden	stump	treehill	room	counter	kitchen	bonsai	truck	train	drjohnson	playroom
3DGS-Compute	Pre-processing	12.84	7.05	10.15	6.94	7.53	3.99	3.02	4.46	3.12	6.29	3.03	7.50	6.04
	Lighting	4.57	3.26	5.19	3.43	3.37	1.84	1.55	3.07	1.40	3.53	2.41	2.61	2.40
	Sorting	246.65	122.68	210.35	180.23	139.98	70.83	50.57	89.96	50.63	105.83	60.83	140.64	110.97
	Rasterization	1239.12*	115.18	608.19*	265.27	147.08	140.16	85.94	177.01	73.43	165.64	130.23	212.10	167.09
	Total	1511.96	253.60	842.15	463.06	303.68	219.31	143.03	277.35	130.58	285.11	198.01	367.93	290.32
3DGS-Graphics	Pre-processing	13.27	7.82	13.73	10.46	8.01	3.40	2.62	4.09	2.62	5.84	2.35	7.22	5.57
	Lighting	5.32	3.66	5.67	3.68	3.80	2.00	1.61	3.55	1.51	4.03	2.68	2.94	2.71
	Sorting	40.26	24.79	38.25	31.09	25.47	11.23	9.47	13.76	9.17	19.16	7.43	23.13	18.43
	Rasterization	618.83*	246.47*	697.81*	344.72*	208.28*	32.50	28.22	52.84	30.86	78.24	39.70	164.25*	82.45
	Total	678.08	283.11	755.89	390.33	245.95	49.46	42.25	74.56	44.47	107.64	52.48	197.86	109.46
LC-WSR	Pre-processing	6.83	3.92	5.53	6.46	4.63	1.94	1.67	2.74	1.64	3.42	1.61	4.61	2.48
	Lighting	4.07	2.81	4.36	3.67	3.23	1.41	1.35	2.98	1.16	3.21	2.31	2.91	1.70
	Rasterization	67.84	28.30	57.84	57.25	52.99	45.44	32.82	68.51	37.52	52.89	48.98	78.11	49.87
	Total	78.99	35.28	67.90	67.63	61.11	49.02	34.06	74.47	40.63	59.75	53.13	85.85	54.28

excellently recovers challenging details of the fireplace in the "Dr Johnson" scenes. In other scenes, WSR particularly recovers better fidelity in areas with strong illumination and reflection.

5.2 COMPUTATIONAL COMPLEXITY STUDY

In this study, we examine the running time and memory consumption of our methods on the mobile devices, using an Snapdragon 8 Gen 3 GPU, and with an implementation based on Vulkan. To make a fair comparison, we also re-implement the 3DGS in Vulkan. Please refer Section 4.4 for implementation details. We conduct our experiments on the Mip-Nerf360, Tanks & Temples, and Deep Blending datasets, where each image is rendered at a resolution of 1920×1080.

Table 2 reports the runtime comparison of 3DGS-Compute, 3DGS-Graphics, and our LC-WSR on the Mip-NeRF360, Tanks&Temples, and Deep Blending datasets. Compared to 3DGS-Compute, 3DGS-Graphics is more efficient as it eliminates the replication steps and thus reducing the number of Gaussians for sorting. Besides 3DGS-Graphics can also better utilize the graphic fixed-functions in the hardware-supported graphic rasterization pipeline. Our method is in most cases faster than the 3DGS-Graphics method due to the elimination of the sorting step and fewer Gaussians. Note that for certain scenes using the 3DGS-Graphics method, we can exhaust our edge device's resources due to the sorting step and high Gaussian count, which will drastically slow down the rasterization step (labeled with "*"). In contrast, our method is fully capable of running all scenes in real-time. In theory, our method's lighting pass should be slightly slower because opacity is calculated using SH, and our rasterization step should be slower due to the weight calculations in the fragment shader and the extra subpass for weight normalization. However, we observed that WSR tends to generate models with fewer Gaussians (scene average 2.88M) compared to the original 3DGS (scene average 3.98M), which is consistent with prior work Radl et al. (2024) that suggests modifying opacity leads to a reduction in the number of Gaussians. This also contributes to faster lighting and rasterization steps for us compared with 3DGS-Graphics. For certain scenes (kitchen and train) that have a similar number of Gaussians, our total time is close to or slightly worse compared to the original model because the overhead added in the rasterization step is not fully compensated by the removal of the sorting step, which may indicate further optimizations are needed for our method's rasterization implementation. Overall, the proposed method is on average 1.23× faster in total time when the mobile resources are not exhausted.

Table 3 compares the memory of our method with 3DGS-Graphics and 3DGS-Compute. Compared to 3DGS-Compute, 3DGS-Graphics utilizes less memory as it performs global sorting thereby elim-

Table 3: Memory (MB) comparison on the Mip-NeRF360, Tanks & Temples and Deep Blending datasets. The images are rendered at a resolution of 1920×1080.

Method	Mip-NeRF360									Tanks & Temples		Deep Blending	
	bicycle	flowers	garden	stump	treehill	room	counter	kitchen	bonsai	truck	train	drjohnson	playroom
3DGS-Compute	2017	1205	1920	1636	1253	542	421	626	429	850	358	1131	851
3DGS-Graphics	1520	911	1448	1235	947	413	322	476	328	644	274	855	645
LC-WSR	881	526	681	853	618	276	241	367	251	439	217	615	344

Table 4: Comparison between WSR methods on the Mip-NeRF360, Tanks & Temples and Deep Blending datasets.

Method	Mip-NeRF 360			Tanks&Temples			Deep Blending		
	PSNR↑	SSIM↑	LPIPS↓	PSNR↑	SSIM↑	LPIPS↓	PSNR↑	SSIM↑	LPIPS↓
DIR-WSR	25.99	0.778	0.262	22.80	0.821	0.218	28.85	0.899	0.254
EXP-WSR	26.97	0.801	0.216	23.32	0.833	0.183	**29.77**	**0.902**	**0.229**
LC-WSR	**27.19**	**0.804**	**0.211**	**23.61**	**0.842**	**0.177**	29.63	**0.902**	**0.229**

inating the replication step. Our method only requires around 63% memory of 3DGS-Graphics. This memory reduction can be attributed to removing the sorting operations as well as fewer total Gaussians. Specifically, removing sorting reduces around 17% memory, while the reducing the number of Gaussians contribute the remaining.

5.3 ABLATION STUDY

Comparison of WSR variants. We compare the variants of WSR in Table 4 on Mip-NeRF360, Tanks & Temples, and Deep Blending datasets. LC-WSR achieved the best performance on Mip-NeRF360 and Tanks & Temples datasets, while EXP-WSR provides the best performance on Deep Blending dataset. See Figure 5 for visual examples that demonstrate LC-WSR performs best at recovering fine details.

Figure 6: Our method eliminates the "popping" artifacts during view transformation.

View dependent opacity. We examine how our method works with view dependent opacity. Experimentally comparing our method with the view independent opacity method used in 3DGS, we demonstrate view dependent opacity can significantly improve the results, shown in Table 5.

Popping artifacts. As a side effect of not relying on sorting, our methods also eliminates "popping" artifacts. Figure 6 shows an experiment in which we slightly rotate the camera, causing the black Gaussian to suddenly "pop" out in 3DGS, generating noticeable temporal artifacts, whereas our method produces temporally consistent results.

Learnable parameters. Traditional OIT methods rely on predefined parameters, while our method optimizes the parameters during training. We compare fixed parameters vs. our learnable parameters in Table 5, which shows that our learnable parameters significantly improve the performance.

6 CONCLUSIONS

This paper introduces a novel sort-free Gaussian Splatting method, enabled by its use of learned non-commutative blend weight functions, a technique we term Weighted Sum Rendering. We presented three variants of Weighted Sum Rendering: DIR-WSR, EXP-WSR, and LC-WSR. These variants effectively eliminate the need for the sort operation in 3DGS. Additionally, we developed a view-dependent opacity technique that significantly enhances reconstruction fidelity in sort-free Gaussian

Table 5: Ablation study on the Mip-NeRF360, Tanks & Temples and Deep Blending datasets.

Method	Mip-NeRF 360			Tanks & Temples			Deep Blending		
	PSNR↑	SSIM↑	LPIPS↓	PSNR↑	SSIM↑	LPIPS↓	PSNR↑	SSIM↑	LPIPS↓
Ours	27.19	0.804	0.211	23.61	0.842	0.177	29.63	0.902	0.229
w.o. learnable parameters	23.19	0.711	0.318	21.55	0.788	0.245	27.92	0.893	0.260
w.o. view-dependent opacity	25.88	0.784	0.251	21.83	0.798	0.237	29.27	0.902	0.249

Splatting. Our experimental results demonstrate that WSR not only achieves competitive visual performance compared to 3DGS but also operates 1.23 times faster on mobile devices.

Limitations and Future Work. **Early-Termination**. In 3DGS a pixel can be easily terminated by monitoring if its accumulated alpha has been saturated. Alternately, we could implement heuristic to halt further evaluation of Gaussians whose opacity falls below some threshold, though our current WSR implementation does not support such an optimization. We implemented our method using the traditional graphics pipeline to make efficient use of mobile GPUs, especially the hardware rasterizer. In our implementation, opacity and weight computations are performed in the fragment shader, while blending is handled by the hardware, since every fragment operates independently and does not have access to the accumulated opacity, we are unable to easily implement early termination. This would require reading the render target's content within the invoking draw pass, which necessitates costly read-modify-write operations and requires Vulkan extensions that many mobile devices do not currently support. Additionally, since the screen-space location of each Gaussian is determined only after the vertex shader, a pixel can only be discarded very late in the pipeline. **Compact Gaussians.** Recently, several compact Gaussian methods have been introduced to significantly reduce the number of Gaussians while maintaining visual performance Jo et al. (2024); Lee et al. (2024); Fan et al. (2023); Niedermayr et al. (2024); Chen et al. (2024); Morgenstern et al. (2023); Navaneet et al. (2023). We believe that our sort-free method can benefit from the rapid pace of research on compact Gaussians.

REFERENCES

Kara-Ali Aliev, Artem Sevastopolsky, Maria Kolos, Dmitry Ulyanov, and Victor Lempitsky. Neural point-based graphics. In *European Conference on Computer Vision*, pp. 696–712. Springer, 2020.

Jonathan T Barron, Ben Mildenhall, Dor Verbin, Pratul P Srinivasan, and Peter Hedman. Mip-nerf 360: Unbounded anti-aliased neural radiance fields. In *Proceedings of the IEEE/CVF conference on computer vision and pattern recognition*, pp. 5470–5479, 2022.

Louis Bavoil, Steven P Callahan, Aaron Lefohn, Joao LD Comba, and Cláudio T Silva. Multi-fragment effects on the gpu using the k-buffer. In *Proceedings of the 2007 symposium on Interactive 3D graphics and games*, pp. 97–104, 2007.

Samuel Rota Bulò, Lorenzo Porzi, and Peter Kontschieder. Revising densification in gaussian splatting. *arXiv preprint arXiv:2404.06109*, 2024.

Loren Carpenter. The a-buffer, an antialiased hidden surface method. In *Proceedings of the 11th annual conference on Computer graphics and interactive techniques*, pp. 103–108, 1984.

Anpei Chen, Zexiang Xu, Andreas Geiger, Jingyi Yu, and Hao Su. Tensorf: Tensorial radiance fields. In *European Conference on Computer Vision (ECCV)*, 2022.

Guikun Chen and Wenguan Wang. A survey on 3d gaussian splatting. *arXiv preprint arXiv:2401.03890*, 2024a.

Guikun Chen and Wenguan Wang. A Survey on 3D Gaussian Splatting, July 2024b. URL http://arxiv.org/abs/2401.03890. arXiv:2401.03890 [cs].

Yihang Chen, Qianyi Wu, Jianfei Cai, Mehrtash Harandi, and Weiyao Lin. Hac: Hash-grid assisted context for 3d gaussian splatting compression. *arXiv preprint arXiv:2403.14530*, 2024.

Zhang Chen, Anpei Chen, Guli Zhang, Chengyuan Wang, Yu Ji, Kiriakos N Kutulakos, and Jingyi Yu. A neural rendering framework for free-viewpoint relighting. In *Proceedings of the IEEE/CVF Conference on Computer Vision and Pattern Recognition*, pp. 5599–5610, 2020.

Zhiqin Chen, Thomas Funkhouser, Peter Hedman, and Andrea Tagliasacchi. Mobilenerf: Exploiting the polygon rasterization pipeline for efficient neural field rendering on mobile architectures. In *The Conference on Computer Vision and Pattern Recognition (CVPR)*, 2023.

Jifeng Dai, Haozhi Qi, Yuwen Xiong, Yi Li, Guodong Zhang, Han Hu, and Yichen Wei. Deformable convolutional networks. In *Proceedings of the IEEE international conference on computer vision*, pp. 764–773, 2017.

Eric Enderton, Erik Sintorn, Peter Shirley, and David Luebke. Stochastic transparency. In *Proceedings of the 2010 ACM SIGGRAPH symposium on Interactive 3D Graphics and Games*, pp. 157–164, 2010.

Cass Everitt. Interactive order-independent transparency. *White paper, nVIDIA*, 2(6):7, 2001.

Zhiwen Fan, Kevin Wang, Kairun Wen, Zehao Zhu, Dejia Xu, and Zhangyang Wang. Lightgaussian: Unbounded 3d gaussian compression with 15x reduction and 200+ fps, 2023.

Zhiwen Fan, Wenyan Cong, Kairun Wen, Kevin Wang, Jian Zhang, Xinghao Ding, Danfei Xu, Boris Ivanovic, Marco Pavone, Georgios Pavlakos, et al. Instantsplat: Unbounded sparse-view pose-free gaussian splatting in 40 seconds. *arXiv preprint arXiv:2403.20309*, 2024.

Ben Fei, Jingyi Xu, Rui Zhang, Qingyuan Zhou, Weidong Yang, and Ying He. 3D Gaussian as a New Era: A Survey. *IEEE Transactions on Visualization and Computer Graphics*, pp. 1–20, 2024. ISSN 1077-2626, 1941-0506, 2160-9306. doi: 10.1109/TVCG.2024.3397828. URL http://arxiv.org/abs/2402.07181. arXiv:2402.07181 [cs].

Sara Fridovich-Keil, Alex Yu, Matthew Tancik, Qinhong Chen, Benjamin Recht, and Angjoo Kanazawa. Plenoxels: Radiance fields without neural networks. In *Proceedings of the IEEE/CVF conference on computer vision and pattern recognition*, pp. 5501–5510, 2022.

Yang Fu, Sifei Liu, Amey Kulkarni, Jan Kautz, Alexei A. Efros, and Xiaolong Wang. Colmap-free 3d gaussian splatting. In *Proceedings of the IEEE/CVF Conference on Computer Vision and Pattern Recognition (CVPR)*, pp. 20796–20805, June 2024.

Abdullah Hamdi, Luke Melas-Kyriazi, Jinjie Mai, Guocheng Qian, Ruoshi Liu, Carl Vondrick, Bernard Ghanem, and Andrea Vedaldi. Ges: Generalized exponential splatting for efficient radiance field rendering. In *Proceedings of the IEEE/CVF Conference on Computer Vision and Pattern Recognition*, pp. 19812–19822, 2024.

Peter Hedman, Julien Philip, True Price, Jan-Michael Frahm, George Drettakis, and Gabriel Brostow. Deep blending for free-viewpoint image-based rendering. 37(6):257:1–257:15, 2018.

Wen Jiang, Boshu Lei, and Kostas Daniilidis. Fisherrf: Active view selection and uncertainty quantification for radiance fields using fisher information. *arXiv preprint arXiv:2311.17874*, 2023.

Joongho Jo, Hyeongwon Kim, and Jongsun Park. Identifying unnecessary 3d gaussians using clustering for fast rendering of 3d gaussian splatting. *arXiv preprint arXiv:2402.13827*, 2024.

Bernhard Kerbl, Georgios Kopanas, Thomas Leimkühler, and George Drettakis. 3D Gaussian Splatting for real-time radiance field rendering. *ACM Transactions on Graphics*, 42(4), 2023.

kishimisu. kishimisu/Gaussian-Splatting-WebGL, September 2024. URL https://github.com/kishimisu/Gaussian-Splatting-WebGL. original-date: 2023-10-19T19:39:24Z.

Arno Knapitsch, Jaesik Park, Qian-Yi Zhou, and Vladlen Koltun. Tanks and temples: Benchmarking large-scale scene reconstruction. *ACM Transactions on Graphics (ToG)*, 36(4):1–13, 2017.

Kevin Kwok. antimatter15/splat, September 2024. URL https://github.com/antimatter15/splat. original-date: 2023-09-11T02:24:56Z.

Joo Chan Lee, Daniel Rho, Xiangyu Sun, Jong Hwan Ko, and Eunbyung Park. Compact 3d gaussian representation for radiance field. In *Proceedings of the IEEE/CVF Conference on Computer Vision and Pattern Recognition*, pp. 21719–21728, 2024.

Zhan Li, Zhang Chen, Zhong Li, and Yi Xu. Spacetime gaussian feature splatting for real-time dynamic view synthesis. In *Proceedings of the IEEE/CVF Conference on Computer Vision and Pattern Recognition (CVPR)*, pp. 8508–8520, June 2024.

Zhong Li, Liangchen Song, Celong Liu, Junsong Yuan, and Yi Xu. Neulf: Efficient novel view synthesis with neural 4d light field. In *Eurographics Symposium on Rendering*, 2022. URL https://api.semanticscholar.org/CorpusID:236913029.

Zhihao Liang, Qi Zhang, Ying Feng, Ying Shan, and Kui Jia. Gs-ir: 3d gaussian splatting for inverse rendering. In *Proceedings of the IEEE/CVF Conference on Computer Vision and Pattern Recognition*, pp. 21644–21653, 2024.

Jiaqi Lin, Zhihao Li, Xiao Tang, Jianzhuang Liu, Shiyong Liu, Jiayue Liu, Yangdi Lu, Xiaofei Wu, Songcen Xu, Youliang Yan, et al. Vastgaussian: Vast 3d gaussians for large scene reconstruction. In *Proceedings of the IEEE/CVF Conference on Computer Vision and Pattern Recognition*, pp. 5166–5175, 2024.

Stephen Lombardi, Tomas Simon, Jason Saragih, Gabriel Schwartz, Andreas Lehrmann, and Yaser Sheikh. Neural volumes: Learning dynamic renderable volumes from images. *ACM Trans. Graph.*, 38(4):65:1–65:14, July 2019.

Tao Lu, Mulin Yu, Linning Xu, Yuanbo Xiangli, Limin Wang, Dahua Lin, and Bo Dai. Scaffold-gs: Structured 3d gaussians for view-adaptive rendering. In *Proceedings of the IEEE/CVF Conference on Computer Vision and Pattern Recognition*, pp. 20654–20664, 2024.

Steve Marschner and Peter Shirley. *Fundamentals of Computer Graphics*. A K Peters, Wellesley, MA, fourth edition, 2015. ISBN 978-1482229394.

Morgan McGuire and Louis Bavoil. Weighted Blended Order-Independent Transparency. *Journal of Computer Graphics Techniques*, 2(4), 2013.

Houman Meshkin. Sort-Independent Alpha Blending, 2007.

Ben Mildenhall, Pratul P. Srinivasan, Matthew Tancik, Jonathan T. Barron, Ravi Ramamoorthi, and Ren Ng. Nerf: representing scenes as neural radiance fields for view synthesis. *Commun. ACM*, 65(1):99–106, dec 2021. ISSN 0001-0782. doi: 10.1145/3503250. URL https://doi.org/10.1145/3503250.

Wieland Morgenstern, Florian Barthel, Anna Hilsmann, and Peter Eisert. Compact 3d scene representation via self-organizing gaussian grids. *arXiv preprint arXiv:2312.13299*, 2023.

Thomas Müller, Alex Evans, Christoph Schied, and Alexander Keller. Instant neural graphics primitives with a multiresolution hash encoding. *ACM Trans. Graph.*, 41(4):102:1–102:15, July 2022. doi: 10.1145/3528223.3530127. URL https://doi.org/10.1145/3528223.3530127.

KL Navaneet, Kossar Pourahmadi Meibodi, Soroush Abbasi Koohpayegani, and Hamed Pirsiavash. Compact3d: Compressing gaussian splat radiance field models with vector quantization. *arXiv preprint arXiv:2311.18159*, 2023.

Thomas Neff, Pascal Stadlbauer, Mathias Parger, Andreas Kurz, Joerg H Mueller, Chakravarty R Alla Chaitanya, Anton Kaplanyan, and Markus Steinberger. Donerf: Towards real-time rendering of compact neural radiance fields using depth oracle networks. In *Computer Graphics Forum*, volume 40, pp. 45–59. Wiley Online Library, 2021.

Simon Niedermayr, Josef Stumpfegger, and Rüdiger Westermann. Compressed 3d gaussian splatting for accelerated novel view synthesis. In *Proceedings of the IEEE/CVF Conference on Computer Vision and Pattern Recognition (CVPR)*, pp. 10349–10358, June 2024.

NVIDIA. *CUB :: CUDA Toolkit Documentation*, 2024. URL `https://docs.nvidia.com/cuda/cub/index.html#cub-overview`. Accessed: 2024-10-23.

Thomas Porter and Tom Duff. Compositing digital images. In *Proceedings of the 11th annual conference on Computer graphics and interactive techniques*, pp. 253–259, 1984.

Minghan Qin, Wanhua Li, Jiawei Zhou, Haoqian Wang, and Hanspeter Pfister. Langsplat: 3d language gaussian splatting. In *Proceedings of the IEEE/CVF Conference on Computer Vision and Pattern Recognition*, pp. 20051–20060, 2024.

Lukas Radl, Michael Steiner, Mathias Parger, Alexander Weinrauch, Bernhard Kerbl, and Markus Steinberger. Stopthepop: Sorted gaussian splatting for view-consistent real-time rendering. *ACM Trans. Graph.*, 43(4), jul 2024. ISSN 0730-0301. doi: 10.1145/3658187. URL `https://doi.org/10.1145/3658187`.

Vincent Sitzmann, Justus Thies, Felix Heide, Matthias Nießner, Gordon Wetzstein, and Michael Zollhofer. Deepvoxels: Learning persistent 3d feature embeddings. In *Proceedings of the IEEE Conference on Computer Vision and Pattern Recognition*, pp. 2437–2446, 2019.

Justus Thies, Michael Zollhöfer, and Matthias Nießner. Deferred neural rendering: Image synthesis using neural textures. *ACM Transactions on Graphics (TOG)*, 38(4):1–12, 2019.

Hugues Thomas, Charles R Qi, Jean-Emmanuel Deschaud, Beatriz Marcotegui, François Goulette, and Leonidas J Guibas. Kpconv: Flexible and deformable convolution for point clouds. In *Proceedings of the IEEE/CVF international conference on computer vision*, pp. 6411–6420, 2019.

Tong Wu, Yu-Jie Yuan, Ling-Xiao Zhang, Jie Yang, Yan-Pei Cao, Ling-Qi Yan, and Lin Gao. Recent advances in 3d gaussian splatting. *Computational Visual Media*, pp. 1–30, 2024.

Chris Wyman. Exploring and expanding the continuum of oit algorithms. In *High Performance Graphics*, pp. 1–11, 2016.

Zhiwen Yan, Weng Fei Low, Yu Chen, and Gim Hee Lee. Multi-scale 3d gaussian splatting for anti-aliased rendering. In *Proceedings of the IEEE/CVF Conference on Computer Vision and Pattern Recognition*, pp. 20923–20931, 2024.

Zehao Yu, Anpei Chen, Binbin Huang, Torsten Sattler, and Andreas Geiger. Mip-splatting: Alias-free 3d gaussian splatting. In *Proceedings of the IEEE/CVF Conference on Computer Vision and Pattern Recognition*, pp. 19447–19456, 2024.

Jiahui Zhang, Fangneng Zhan, Muyu Xu, Shijian Lu, and Eric Xing. Fregs: 3d gaussian splatting with progressive frequency regularization. In *Proceedings of the IEEE/CVF Conference on Computer Vision and Pattern Recognition*, pp. 21424–21433, 2024.

Zi-Xin Zou, Zhipeng Yu, Yuan-Chen Guo, Yangguang Li, Ding Liang, Yan-Pei Cao, and Song-Hai Zhang. Triplane meets gaussian splatting: Fast and generalizable single-view 3d reconstruction with transformers. In *Proceedings of the IEEE/CVF Conference on Computer Vision and Pattern Recognition*, pp. 10324–10335, 2024.

A   Implementation details on mobile phones

For the 3DGS-Graphic method, the pre-processing and the lighting steps remain the same as the original 3DGS implementation except for that they are now written in GLSL compute shaders. We changed the rasterization step from a compute based pipeline to traditional graphic pipeline using instanced draw, where each Gaussian treated as an instance and covered by a triangle pair in vertex shader. The fragment shader then colors the pixels within a Gaussian's radius. The alpha blending is handled by the hardware automatically at the rendering back-end. With the graphic pipeline, all Gaussians are rendered using a single instanced draw call instead of the per-tile fashion used by 3DGS. The sorting step is also changed from a tile-based sort to global sort, which is implemented using GLSL compute shader.

For our method, the pre-processing and the lighting stages remain the same as the 3DGS method in Vulkan except for that now opacity is calculated in the lighting stage based on camera view and SHs. Sorting step is removed and we also pass depth for each Gaussian to the graphic pipeline to calculate the per-Gaussian weight. The alpha blending operation is changed from using the blending factor to simple summation of the color and weight. We added an extra graphic pass using the Vulkan subpass feature to handle the final normalization. To make the 3DGS-Graphic method and our method a fair comparison, the render target for both is set to use 16-bit RGBA. Note that the original 3DGS can be implemented using 8-bit RGBA with a slightly lower image quality and better rendering speed, but because our method requires the color and weight to be accumulated, we used 16-bit to avoid overflow issue.

B   Per Scenes Evaluation Metric

Table 6, 7, and 8 present the PSNR, SSIM, and LPIPS metrics for each scene within Mip-NeRF360, Tanks & Temples, and Deep Blending datasets, respectively.

Table 6: PSNR scores of our method on the Mip-NeRF360 dataset, the Tanks&Temples dataset, and the Deep Blending dataset.

Method	Mip-NeRF360										Tanks&Temples			Deep Blending		
	bicycle	flowers	garden	stump	treehill	room	counter	kitchen	bonsai	Avg	truck	train	Avg	drjohnson	playroom	Avg
Plenoxels	21.91	20.10	23.49	20.66	22.25	27.59	23.62	23.42	24.67	23.08	23.22	18.93	21.08	23.14	22.98	23.06
INGP-Base	22.19	20.35	24.60	23.63	22.36	29.27	26.44	28.55	30.34	25.30	23.26	20.17	21.72	27.75	19.48	23.62
INGP-Big	22.17	20.65	25.07	23.47	22.37	29.69	26.69	29.48	30.69	25.59	23.38	20.46	21.92	28.26	21.67	24.96
Mip-NeRF360	24.31	**21.65**	26.88	26.18	**22.93**	31.47	**29.45**	**31.99**	**33.40**	**27.69**	24.91	19.52	22.22	29.14	29.66	29.40
3DGS	**25.25**	21.52	27.41	**26.55**	22.49	30.63	28.70	30.32	31.98	27.21	25.18	21.09	23.14	28.77	**30.04**	29.41
Ours-LC	24.20	20.45	**27.78**	25.39	22.01	**31.93**	29.53	31.38	32.05	27.19	**25.28**	**21.93**	**23.61**	**29.25**	30.00	**29.63**

Table 7: SSIM scores of our method on the Mip-NeRF360 dataset, the Tanks&Temples dataset, and the Deep Blending dataset.

Method	Mip-NeRF360										Tanks&Temples			Deep Blending		
	bicycle	flowers	garden	stump	treehill	room	counter	kitchen	bonsai	Avg	truck	train	Avg	drjohnson	playroom	Avg
Plenoxels	0.496	0.431	0.606	0.523	0.509	0.8417	0.759	0.648	0.814	0.626	0.774	0.663	0.719	0.787	0.802	0.795
INGP-Base	0.491	0.450	0.649	0.574	0.518	0.855	0.798	0.818	0.890	0.671	0.779	0.666	0.723	0.839	0.754	0.797
INGP-Big	0.512	0.486	0.701	0.594	0.542	0.871	0.817	0.858	0.906	0.699	0.800	0.689	0.745	0.854	0.779	0.817
Mip-NeRF360	0.685	0.583	0.813	0.744	0.632	0.913	0.894	0.920	**0.941**	0.792	0.857	0.660	0.759	0.901	0.900	0.901
3DGS	0.771	**0.605**	0.868	**0.775**	**0.638**	0.914	0.905	0.922	0.938	**0.815**	0.879	**0.802**	0.841	**0.899**	**0.906**	**0.903**
Ours	**0.744**	0.580	**0.872**	0.728	0.614	**0.925**	**0.909**	**0.923**	0.938	0.804	**0.882**	**0.802**	**0.842**	0.898	**0.906**	0.902

Table 8: LPIPS scores of our method on the Mip-NeRF360 dataset, the Tanks&Temples dataset, and the Deep Blending dataset.

Method	Mip-NeRF360										Tanks&Temples			Deep Blending		
	bicycle	flowers	garden	stump	treehill	room	counter	kitchen	bonsai	Avg	truck	train	Avg	drjohnson	playroom	Avg
Plenoxels	0.506	0.521	0.386	0.503	0.540	0.4186	0.441	0.447	0.398	0.463	0.335	0.422	0.379	0.521	0.499	0.510
INGP-Base	0.487	0.481	0.312	0.450	0.489	0.301	0.342	0.254	0.227	0.371	0.274	0.386	0.330	0.381	0.465	0.423
INGP-Big	0.446	0.441	0.257	0.421	0.450	0.261	0.306	0.195	0.205	0.331	0.249	0.360	0.305	0.352	0.428	0.390
Mip-NeRF360	0.301	0.344	0.170	0.261	0.339	0.211	0.204	0.127	0.176	0.237	0.159	0.354	0.257	0.237	0.252	0.245
3DGS	**0.205**	**0.336**	0.103	**0.210**	0.317	0.220	0.204	0.129	0.205	0.214	0.148	**0.218**	0.183	0.244	0.241	0.243
Ours	**0.205**	0.342	**0.097**	0.235	**0.311**	**0.197**	**0.191**	**0.125**	0.199	**0.211**	**0.136**	0.219	**0.177**	**0.233**	**0.225**	**0.229**